

Self-assembly beyond semifluorinated alkanes in a semifluorinated benzene derivative†

Cite this: *Soft Matter*, 2013, **9**, 11334

René Stangenberg,^a Christos Grigoriadis,^b Dirk Schneider,^a Hans-Jürgen Butt,^a George Fytas,^{a,c} Klaus Müllen^a and George Floudas^{*b}

Tethering amphiphiles symmetrically to a small benzene core – in analogy to semifluorinated alkanes (SFAs) – gives rise to self-assembly far more rich than any previously investigated SFA. The modulation of intermolecular interactions between hydrocarbon and fluorocarbon chains as well as additional π – π interactions of the cores are thought to be responsible for the rich self-assembly. The system is investigated with respect to thermodynamics, structure and dynamics, respectively, with differential scanning calorimetry, X-ray scattering and dielectric spectroscopy. The mechanical and nano-mechanical properties are studied with rheology and Brillouin light scattering covering a broad frequency range and spatial resolution. Starting from lower temperatures distinct phases are identified consisting of nanophase separated domains comprising crystalline or melted fluorocarbon/hydrocarbon domains. At intermediate temperatures lamellar phases are identified with molecular and supramolecular order. At higher temperatures domains composed of thermodynamically unfavorable yet kinetically mixed configurations exist. The latter phase is prone to annealing as these trapped configurations convert from locally segregated to more homogeneously mixed molecules. At higher temperatures a quasi-isotropic phase is formed composed of orientationally correlated dipoles.

Received 7th August 2013

Accepted 11th October 2013

DOI: 10.1039/c3sm52125g

www.rsc.org/softmatter

1. Introduction

Fluorocarbons have a range of applications that rely on their special physical properties, such as high thermal and chemical stability, low surface tension, high fluidity and density, high compressibility, low dielectric constant and refractive index, high vapor pressure and high gas solubilities.^{1–3} Additionally, they are more hydrophobic than hydrocarbon chains and at the same time are oleophobic. These intriguing features reflect the atomic characteristics of fluorine with a larger van der Waals radius than hydrogen (0.147 nm vs. 0.12 nm) and high electronegativity. As a result fluorocarbon chains are bulky and stiff, usually in a helical conformation as opposed to the planar zig-zag conformation of hydrocarbon chains.^{1,2} Despite the strong intra-molecular interactions, fluorocarbons display weak intermolecular interactions; this originates from the low

polarizability of fluorine that gives rise to weaker van der Waals interactions. The pronounced intramolecular rigidity and intermolecular fluid-like behavior are reflected, respectively, by the higher melting and reduced boiling points as compared to hydrocarbons.¹

Partially fluorinated compounds can enhance self-assembly through the fluorophobic effect, *i.e.*, the mutual thermodynamic incompatibility between hydrocarbon and fluorocarbon chains.^{1–5} The size mis-match between hydrocarbon and fluorocarbon chains further enhances incompatibility. The smallest partially fluorinated compounds are diblock copolymers of semifluorinated alkanes (SFAs), with the chemical structure $F(CF_2)_m(CH_2)_nH$, or shortly F_mH_n .^{5–10} The incompatibility and cross-sectional incommensurability of the fluorocarbon and hydrocarbon blocks favor bilayered lamellae that best minimize the heterocontacts and allow for hydrocarbon segments to adjust their density through interdigitation. Indeed, a recent investigation of the SFA $F_{12}H_{12}$ has shown that the low temperature phase is composed of bilayered lamellae with an interdigitated hydrocarbon layer.¹¹ However, at higher temperatures, a monolayer lamellar phase was formed that co-exists with a liquid phase. A model was proposed based on a two-stage melting mechanism: one initiated at the film surface and another from the grain-boundary/crystallite surface.¹¹ More complex structures were also investigated consisting of biphasic fluorocarbon/hydrocarbon amphiphiles tethered to cores at distances commensurate with their packing requirement.^{12,13} It

^aMax Planck Institute for Polymer Research, D-55128 Mainz, Germany

^bDepartment of Physics, University of Ioannina, 45110 Ioannina, Greece. E-mail: gfloudas@cc.uoi.gr

^cDepartment of Materials Science, University of Crete and FORTH, 71110-Heraklion, Greece

† Electronic supplementary information (ESI) available: The purity of all compounds was proven by NMR and FD-MS; as observable all starting material is converted and no other impurities remain; before the physical measurement the complete removal of all solvent was proven by NMR in another solvent, and the stability and the persistency of the compounds were proven after each experiment by NMR (no decomposition was detectable). See DOI: 10.1039/c3sm52125g

was shown that such molecules can exhibit different rotation conformational isomers with kinetically trapped fluorocarbon and hydrocarbon chains. The addition of a minor component of a smaller molecule had a drastic effect in unlocking the mixed conformations by providing thermodynamic pathways towards equilibrium.^{12,13}

Tethering amphiphiles symmetrically to a small benzene core modulates the local interactions between hydrocarbon and fluorocarbon chains and introduces additional π - π interactions that can enhance the self-assembly. The molecule has to satisfy not only the unfavourable hydrocarbon-fluorocarbon interactions but also the strong π - π interactions. Herein we report the synthesis of a new amphiphile of 1-dodecyl-4-(perfluorododecyl) benzene (**3**) and explore the phase behaviour and dynamics in comparison to 1,4-dodecylbenzene (**4**). Fluorous solvents commonly exhibit temperature-dependent miscibilities with organic solvents, but mostly are immiscible. In nonaqueous fluorous emulsions used in polymerization reactions, surfactants with a lipophilic and fluorophilic tail are a necessity. This requires the synthesis of such amphiphiles and in depth understanding of their phase behavior. Compound **3**, in particular, can easily be produced at large scales suitable for industrial purposes. We employ thermodynamic (DSC), structural (X-rays) and dynamic probes. The latter are based on dielectric spectroscopy (DS) that follows the dipole dynamics, and rheology, Brillouin Light Scattering (BLS) to follow the mechanical response and nano-mechanical properties spanning a frequency range from 0.1 Hz to GHz. We find that the phase behaviour of **3** is far more rich when compared to 1,4-dodecylbenzene (**4**) or to the analogous $F_{12}H_{12}$. The structure now includes nanophase separated domains comprising crystalline or melted fluorocarbon/hydrocarbon domains, lamellar phases with molecular and supramolecular order as well as domains composed of thermodynamically unfavourable yet kinetically mixed configurations that appear sequentially with increasing temperature. Lastly, the nature of the isotropic phase is explored.

2. Experimental

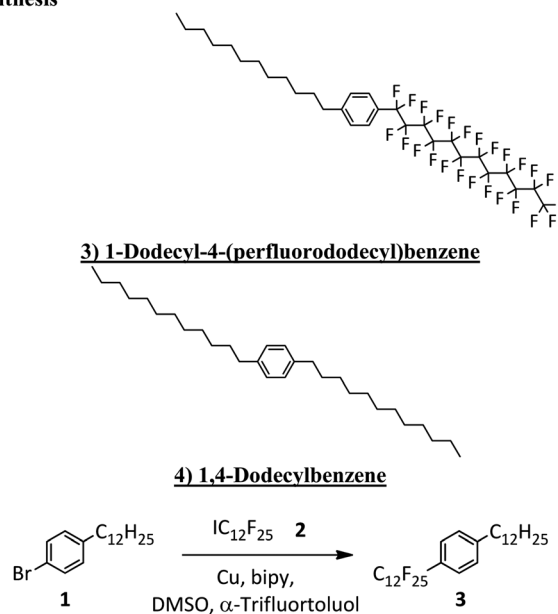
(a) Synthesis

Experimental methods. Perfluorododecyl iodide (Sigma), copper-powder (Sigma), 2,2'-bipyridine (Sigma) and 1-bromo-4-dodecylbenzene (ABCR) were used directly without further purification. For all reactions dry solvents were used (Scheme 1).

Synthetic procedure

1-Dodecyl-4-(perfluorododecyl)benzene (3). A solution of 1-bromo-4-dodecylbenzene **1** (0.435 g, 1.34 mmol), $C_{12}F_{25}I$ **2** (1 g, 1.34 mmol), copper powder (0.172 g, 2.68 mmol) and 2,2'-bipyridine (0.015 g, 0.09 mmol) in α,α,α -trifluorotoluene (30 mL) and DMSO (10 mL) was heated for 96 h at 80 °C before it was poured into a beaker containing dichloromethane (100 mL) and water (100 mL).^{14,15} The organic layer was separated, washed three times with water and dried over $MgSO_4$. The crude product was purified *via* column chromatography (silica, pure hexane as eluent) to yield 879 mg (76%) of a white solid.

(a) Synthesis



Scheme 1 Structures of the target molecules **3** and **4**; reaction scheme of Ullmann-coupling to obtain **3**.

m/z (FD-MS) 863.2 (100%); 1H -NMR (500 MHz, THF) = δ_H 7.38 (d, 2H, $J = 9$ Hz, Ar-H), 7.09 (d, 2H, $J = 9$ Hz, Ar-H), 2.56 (t, 2H, $J = 6$ Hz, Ar- CH_2 -), 1.59 (q, 2H, $J = 6$ Hz, $-CH_2$ -), 1.30–1.27 (m, 18H, Alkyl- CH_2 -), 0.89 (t, 3H, $J = 6$ Hz, $-CH_3$); ^{13}C -NMR (125 MHz, THF) = δ_C 142.26, 142.11, 142.00, 132.76, 131.31, 130.32, 130.15, 127.32, 124.48, 120.39, 119.98, 119.35, 119.23, 110.35, 108.71, 36.12, 35.30, 31.86, 31.03, 29.82, 29.57, 29.49, 29.38, 29.24, 29.17, 22.60, 13.99; ^{19}F -NMR (470 MHz, THF) = δ_F -108.88, -112.38, -116.24, -119.61, -119.96, -120.37, -120.54, -121.41, -122.04, -124.94, -128.14, -137.12, -137.23.

1,4-Dodecylbenzene (4). 1,4-Dodecylbenzene (**4**) was obtained from commercial sources and was purified *via* recrystallization from methanol before use.

(b) Differential scanning calorimetry (DSC)

The thermal behavior was studied by differential scanning calorimetry on cooling and subsequent heating at a rate of 10 K min^{-1} , with a Mettler 30 DSC. The DSC traces from the second cooling and heating scans of compounds **3** and **4** are shown in Fig. 1. The transition temperatures and associated heats of fusion on cooling and subsequent heating are summarized in Table 1. The effect of annealing on the high temperature features of compound **3** was studied. This is discussed together with the BLS data below.

(c) Polarizing optical microscopy (POM)

A Zeiss Axioskop 40, equipped with a video camera and a fast frame grabber, was used to follow the structural changes of the two samples. The samples were placed between microscopy slides with a distance of 25 μm provided by Teflon spacers. A Linkam temperature control unit (THMS600), equipped with a

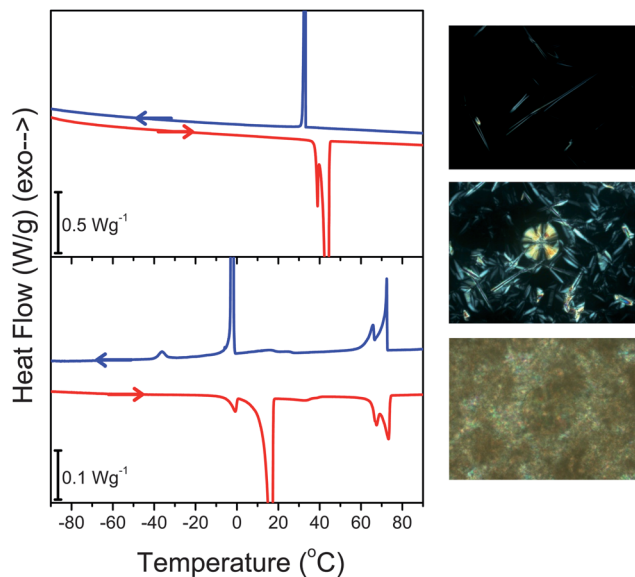


Fig. 1 (Left) DSC traces of 1,4-dodecylbenzene **4** (top) and **3** (bottom) on cooling (blue trace) and subsequent heating (red trace) with 2 °C min^{-1} . (Right) POM images of **3** obtained on cooling from the melt (rate 0.1 °C min^{-1}) that correspond to temperatures 55.6 °C (top), 30.0 °C (middle) and 1.0 °C (bottom). Notice the coexisting crystal structures at 30.0 °C and the crystallization at the lower temperature. The images have dimensions of $694\text{ }\mu\text{m} \times 520\text{ }\mu\text{m}$.

TMS94 temperature programmer, was employed for the temperature-dependent studies. Images were recorded following slow cooling (0.1 and 1 °C min^{-1}) from the melt state. Representative POM images are shown in Fig. 1.

(d) X-ray scattering

Wide-angle and medium angle X-ray scattering (WAXS/MAXS) measurements were made using Cu K α radiation from a Rigaku MicroMax 007 X-ray generator, using Osmic Confocal Max-Flux curved multilayer optics. Samples in the form of fibers were prepared with a mini-extruder at 10 °C .¹⁶ In both cases, the X-ray beam was perpendicular to the fiber axis. Temperature dependent WAXS/MAXS measurements were performed at temperatures in the range from -40 °C to 70 °C on cooling and subsequent heating. A waiting (equilibration) time of 1800 s and a measurement time of 1800 s were set in the temperature programme. Diffraction patterns were obtained by radial averaging of the data recorded by a 2D-detector (Mar345 Image Plate).

(e) Dielectric spectroscopy (DS)

Dielectric measurements were carried out with a Novocontrol Alpha frequency analyzer under “isobaric” conditions as a function of temperature. Measurements were performed at different temperatures in the range 213.15 – 453.15 K in steps of 5 K , at atmospheric pressure, and for frequencies in the range from 10^{-2} to 10^7 Hz . The complex dielectric permittivity $\epsilon^* = \epsilon' - i\epsilon''$, where ϵ' is the real and ϵ'' is the imaginary part, has been obtained as a function of frequency ω , and temperature T , i.e., $\epsilon^*(T, \omega)$.^{17–19} The analysis of the T -dependent experiments was made using the empirical equation of Havriliak and Negami (HN):²⁰

$$\epsilon_{\text{HN}}^*(\omega, T) = \epsilon_{\infty}(T) + \frac{\Delta\epsilon(T)}{[1 + (i\omega\tau_{\text{HN}}(T))^m]^n} + \frac{\sigma_0(T)}{i\epsilon_f\omega} \quad (1)$$

where $\epsilon_{\infty}(T)$ is the high-frequency permittivity, $\tau_{\text{HN}}(T)$ is the characteristic relaxation time in this equation, $\Delta\epsilon(T) = \epsilon_0(T) - \epsilon_{\infty}(T)$ is the relaxation strength, m and n (with limits $0 < m, mn \leq 1$) describe respectively the symmetrical and asymmetrical broadening of the distribution of relaxation times, σ_0 is the dc conductivity, and ϵ_f is the permittivity of free space. From τ_{HN} , the relaxation time at maximum loss, τ_{max} , is obtained analytically following

$$\tau_{\text{max}} = \tau_{\text{HN}} \sin^{-1/m} \left(\frac{\pi m}{2(1+n)} \right) \sin^{1/m} \left(\frac{\pi mn}{2(1+n)} \right) \quad (2)$$

The measured ϵ'' spectra and the derivative of ϵ' ($d\epsilon'/d \ln \omega \sim -(2/\pi)\epsilon''$) have been used for the analysis of the dynamic behavior with respect to the fluorocarbon dipole. The rates of ionic motion (ion mobility) were determined by the analysis of the complex electric modulus $M^* = M' + iM''$, which is related to the complex dielectric permittivity as $M^* = 1/\epsilon^*$. In particular the characteristic time of ion motion was extracted from the position of the maximum value in M'' . Alternatively, the characteristic time can be obtained from the crossing of the real and imaginary parts. The two methods give identical relaxation times for narrow (Debye) processes but differ for broader processes. Some representative fits to the dielectric loss spectra of compound **3** at selected temperatures are given in the ESI.†

(f) Rheology

An Advanced Rheometric Expansion System (ARES) equipped with a force-rebalanced transducer was used in the oscillatory mode. Depending on the temperature range two transducers were employed with $2000, 2\text{ g cm}$ and $200, 0.2\text{ g cm}$ upper and lower sensitivity, respectively. Measurements were made with

Table 1 Transition temperatures and associated heats on cooling and subsequent heating runs (rate 10 °C min^{-1}) of compound **3**

Phase transition	Structural change	Transition temperature ($^{\circ}\text{C}$)	ΔH (J g^{-1})
1	Formation/melting	70.8/74.4	12.0/11.9
2	Formation/melting	64.0/67.9	5.0/4.1
3	Lamellae (L1, L2) formation/melting	From -7 to 20 /from 25 to 40	1.46/0.44
4	Fluorocarbon crystallization/melting	$-1.4/17.9$	40.0/42.1
5	Hydrocarbon crystallization/melting	$-38.9/-0.24$	1.3/1.3

the environmental test chamber as a function of temperature. The sample was prepared on the lower plate of the 10 mm diameter parallel plate geometry setup and heated under a nitrogen atmosphere until it could flow. Subsequently, the upper plate was brought into contact, the gap thickness was adjusted to 1 mm, and the sample was slowly cooled to the desired starting temperature. The storage (G') and loss (G'') shear moduli were monitored in different types of experiments. First, the linear and nonlinear viscoelastic ranges were identified, by recording the strain amplitude dependence of the complex shear modulus $|G^*|$ at selected temperatures. In subsequent experiments strain amplitudes within the linear viscoelastic range were used. These experiments involved isochronal temperature scans (at $\omega = 10 \text{ rad s}^{-1}$) on cooling and subsequent heating and isothermal frequency scans within the range $10^{-1} < \omega < 10^2 \text{ rad s}^{-1}$ at some selected temperatures ($T = 0 \text{ }^\circ\text{C}$ and $30 \text{ }^\circ\text{C}$).

(g) Brillouin Light Scattering (BLS)

BLS is a non-destructive and non-contact optical technique to access acoustic or elastic properties probing thermally activated propagating phonons and localized vibration modes in bulk as well as nanostructured materials in the hypersonic frequency regime (GHz). Hence, BLS is a sensitive tool to study structure, morphology and phonon-matter interactions in composite materials,²¹ provided that the phonon wavelength $2\pi/q$ ($q = (4\pi n/\lambda)\sin(2\theta/2)$, where λ is the wavelength, n is the refractive index and 2θ is the scattering angle) commensurates their characteristic (periodic) spacing d , *i.e.*, $qd \sim 1$. BLS relies on the interaction between single mode incident photons with wave vector, k_i , and thermally excited phonons $q = k_s - k_i$ along a specified direction determined by the scattering geometry (k_s is the wave vector of the scattered photons). The exchanged phonon energy is represented by the frequency shift, ω , of the inelastically scattered light, known as the Brillouin doublet. These small shifts (few GHz) are resolved by an actively stabilized tandem FP interferometer. The heatable cell holder in the midst of a goniometer carrying the laser source (532 nm) allows for temperature- and q -dependent acoustic measurements at the mesoscale.²² Herein, BLS is used to track the phase changes

of compound **3** manifested in the longitudinal sound velocity, c_L . The temperature dependence of c_L sensitively reflects phase transitions accompanied with changes in the mechanical impedance, $Z = \rho c_L$, with ρ being the mass density. Typical accumulation times for Brillouin spectra in the bulk system under study range from 1 to 30 min. The thermal history of the samples A1–C used in BLS is provided in Table 2.

3. Results

(a) Thermodynamics of phase transitions

The DSC traces of compounds 1-dodecyl-4-(perfluorododecyl)-benzene (**3**) and 1,4-dodecylbenzene (**4**) are compared in Fig. 1. The single crystallization process in **4** is replaced by several order-to-order transitions in **3**. It is our main task to characterize the phases and to explore the molecular dynamics together with the mechanical response of each phase. When cooling from $80 \text{ }^\circ\text{C}$ (in the isotropic phase), the POM images of **3** (Fig. 1) display distinct structural changes. At $55.6 \text{ }^\circ\text{C}$ needle-like objects start to grow, whereas at $30.0 \text{ }^\circ\text{C}$ some spherulitic objects appear that grow at a slower rate. At $1.0 \text{ }^\circ\text{C}$ the specimen undergoes crystallization. These transitions seen by POM relate also to the thermodynamic state of the system as further revealed by BLS in Section IIIC. Despite the absence of any birefringence in POM at temperatures above $56.6 \text{ }^\circ\text{C}$, the DSC trace obtained on cooling exhibits two well-resolved exothermic peaks centered at 70.8 and $64.0 \text{ }^\circ\text{C}$. On further cooling a broad exotherm from 20 to $-7 \text{ }^\circ\text{C}$ exists that associates with the dual growing superstructures seen in POM. At $-1.4 \text{ }^\circ\text{C}$ the narrow and intense exotherm reflects the crystallization also seen in POM. At even lower temperatures, a shallow exotherm is seen at $-38.9 \text{ }^\circ\text{C}$ only in DSC. On heating all transitions reveal hysteresis but this effect is stronger for the low-temperature transitions (Table 1). As we will discuss below, this reflects the confined crystallization of hydrocarbon and fluorocarbon chains at the lower temperatures. Fig. 2 provides a schematic of the different phases of compound **3** obtained from a combination of X-rays, DSC, POM, rheology and BLS (to be discussed in detail below) as a function of temperature.

Table 2 Thermal history of the samples used for the temperature scans of the BLS experiment with pertinent observations (in parenthesis) as presented in Fig. 9 and 10

Code	Thermal treatment ^a
A1 as prepared: black squares, Fig. 10 A2 annealed: brown squares, Fig. 9	Heated from $23 \text{ }^\circ\text{C}$ to $125 \text{ }^\circ\text{C}$ (prominent dip), then slowly cooled to $23 \text{ }^\circ\text{C}$ Then A1 heated from $23 \text{ }^\circ\text{C}$ to $113 \text{ }^\circ\text{C}$ (no dip); reproducibility (not shown) revealed
B1 as prepared: red circles, Fig. 10 B2 annealed: green circles, Fig. 9	Heated from $23 \text{ }^\circ\text{C}$, annealed at $77 \text{ }^\circ\text{C}$ up to 18 hours (strong time dependence), then slowly cooled to $23 \text{ }^\circ\text{C}$ Then B1 heated to $95 \text{ }^\circ\text{C}$, cooled to $11 \text{ }^\circ\text{C}$ (open symbols) and subsequently heated to $91 \text{ }^\circ\text{C}$ (solid symbols)
C as prepared: blue triangles, Fig. 9	Annealed for 20 min at $93 \text{ }^\circ\text{C}$, stepwise ($\sim 10 \text{ K h}^{-1}$) cooled to $-9 \text{ }^\circ\text{C}$ and subsequently heated to $96 \text{ }^\circ\text{C}$ (at $\sim 10 \text{ K h}^{-1}$).

^a All samples were heated to $80 \text{ }^\circ\text{C}$ (above the melting point) for a few seconds prior to the first measurement to increase the transmission (less grain boundaries). The heating cycles were not continuous. At each temperature the sample was allowed to equilibrate for 15–20 min and subsequently the BLS spectrum was recorded for about 15 min.

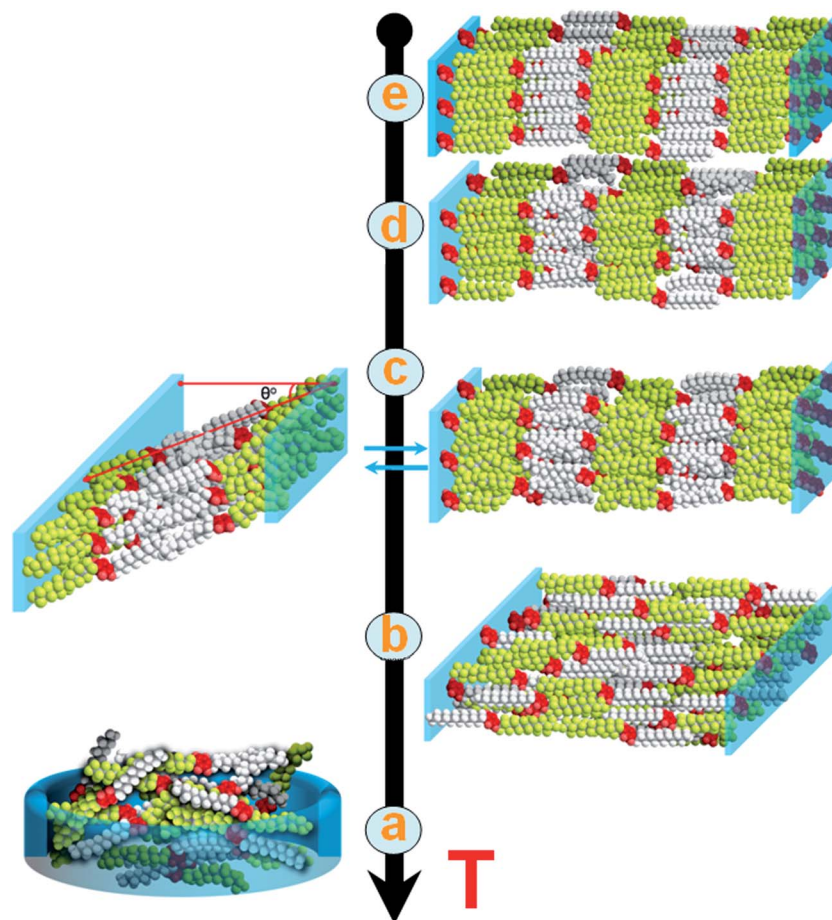


Fig. 2 Schematic illustration of the different phases of $F(CF_2)_{12}Ph(CH_2)_{12}H$ (CF_2 -block in green) obtained on heating: (e) low temperature lamellar phase comprising crystalline fluorocarbon and hydrocarbon parts, (d) lamellar phase comprising melted hydrocarbon chains, (c) coexisting phases of tilted and non-tilted lamellar structures comprising melted hydrocarbon and fluorocarbon chains, (b) mixed domains each composed of hydrocarbon/fluorocarbon chains and (a) quasi-isotropic phase composed of orientationally correlated dipoles. The vertical arrow gives the direction of increasing temperature but serves also as the fiber axis orientation.

Understanding the origin of the thermodynamic (DSC) and optical (POM) transitions requires knowledge of the underlying structural changes. Before we comment on the structural changes we discuss the temperature dependence of the dielectric permittivity and of the viscosity that can also be used to elucidate the morphological transitions. The temperature dependence of the dielectric permittivity of compound **3** under isochronal conditions (Fig. 3), obtained on cooling and subsequent heating, shows distinct changes at the respective phase transitions. On cooling from 100 °C, ϵ' increases with decreasing temperature and changes slope at around 55 °C to a less steep T -dependence. The static dielectric constant of polar liquids with short-range interactions between molecules has been the subject of a theory by Kirkwood and later by Fröhlich.^{17,18} The theory has considered an infinite continuum of dielectric permittivity, ϵ'_s , and within this a spherical region containing N_0 elementary dipoles that were treated explicitly was observed. Based on these assumptions, the dielectric permittivity can be expressed as:

$$\epsilon'_s = \epsilon_\infty + \frac{1}{3\epsilon_o} Fg \frac{\mu^2}{k_B T} \frac{N_0}{V} \quad (3)$$

Here, $F = \epsilon'_s(\epsilon_\infty + 2)^2/[2(\epsilon'_s + \epsilon_\infty)]$ is the local field, N/V is the number density of dipoles expressed as $(\rho/M)N_A$, where ρ is the mass density (defined above) and M is the molar mass, μ is the dipole moment and g is the dipole orientation correlation function

$$g = 1 + \frac{\left\langle \sum_{i=1}^{N_0} \sum_{i < j} \mu_i \mu_j \right\rangle}{N_0 \mu^2} \quad (4)$$

Considering only nearest neighbor orientation correlations, eqn (4) for the reference dipole surrounded by z equivalent nearest neighbors reduces to $g = 1 + z\langle \cos \theta \rangle$. Here, θ is the angle between the reference dipole and one of its z nearest neighbors. We have employed eqn (3) and (4) with $\rho = 1.43 \text{ g cm}^{-3}$ and $\mu = 4.5 \text{ D}$ (program MOPAC, PM6) and fitted the $\epsilon'_s(T)$ dependence within the temperature ranges from 100 to 55 °C and from 38 to 28 °C. The resulting dipole orientation correlation function, g , assumes 0.25 and 0.19, respectively, indicating that dipoles have preferred orientation correlations that persist at high temperatures. These dipole-dipole correlations presumably bring some fluorocarbon chains in proximity but due to their short range do not show up in POM

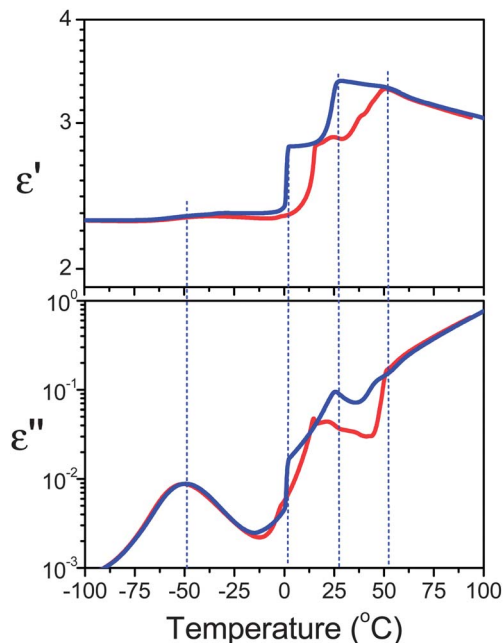


Fig. 3 Isochronal measurements ($f = 1154$ Hz) of the dielectric permittivity (top) and loss (bottom) of compound **3** obtained on cooling (in blue) and subsequent heating (in red) with $2\text{ }^{\circ}\text{C min}^{-1}$. The vertical lines indicate the different transition temperatures obtained on cooling.

(Fig. 1) or WAXS (see below). On further cooling, the dielectric permittivity decreases in steps reflecting the phase transformations. A smaller step at around $-50\text{ }^{\circ}\text{C}$ and the associated maximum in the loss curve reflect molecular relaxation based on the dielectric loss maximum, to be discussed with respect to Fig. 8.

Fig. 4 is a composite plot where the thermodynamic transitions are compared with their dielectric and viscoelastic counterparts. The different cooling rates in DSC, DS and rheology ($2, 2$ and $0.5\text{ }^{\circ}\text{C min}^{-1}$, respectively) give somewhat different transition temperatures. Nevertheless, the transitions (indicated with numbers) and the corresponding morphological regimes (indicated with letters) can clearly be identified. Starting from higher temperatures, the dual transition indicated as “1” and “2” might relate to transformations between different configurations that bring some fluorocarbon chains in proximity to hydrocarbon chains, *i.e.*, lamellae with mixed configurations (to be discussed below). These thermodynamically unfavorable yet kinetically trapped states give rise to exothermic peaks observed in DSC and to changes in the local dipole correlations reflected in the broad maximum of the absolute derivative of the dielectric permittivity with respect to temperature (middle panel of Fig. 4). However, these microstate transformations do not show up in WAXS because of the low contrast in the electron density of the formed domains emphasizing the necessity of the different techniques.

The broad DSC transition indicated as “3” is accompanied with a strong dielectric activity and a step-wise increase in viscosity. As we will see below from Fig. 5, within this temperature range significant structural changes at the molecular and supramolecular level take place that can be

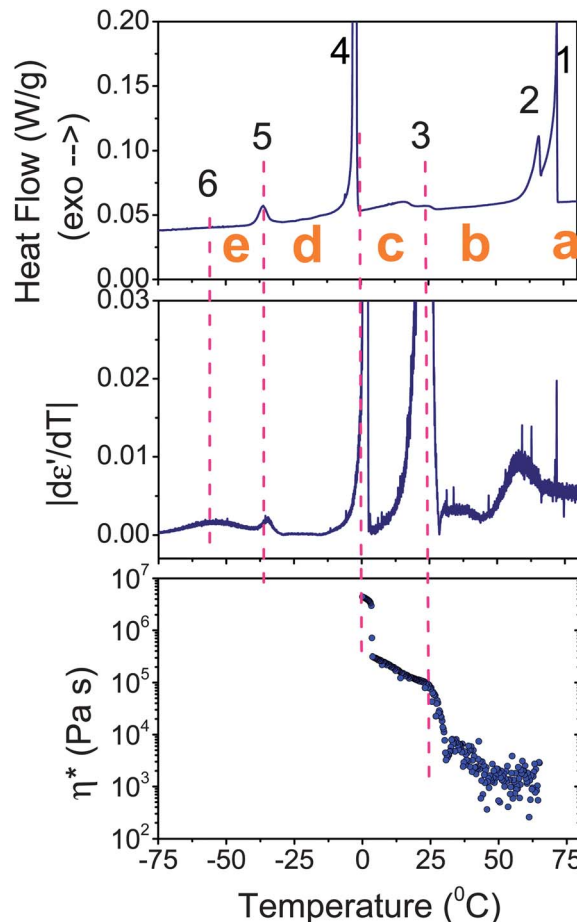


Fig. 4 Temperature dependence of the heat flow (DSC) (top), absolute derivative of the dielectric permittivity (middle) and viscosity (bottom) of compound **3** obtained on cooling with respective rates of $2, 2$ and $0.5\text{ }^{\circ}\text{C min}^{-1}$. Numbers and vertical lines indicate phase transitions: (1)/(2) formation of mixed configurations of fluorocarbon/hydrocarbon chains, (3) coexisting unit cells comprising tilted (non-interdigitated) and non-tilted but nearly fully interdigitated hydrocarbon and fluorocarbon domains, (4) crystallization of fluorocarbon chains, (5) crystallization of hydrocarbon chains and (6) glass temperature. Letters indicate the different phases in conjunction with Fig. 2.

identified by WAXS. These reflect the nano-phase separated hydrocarbon and fluorocarbon domains with an increased purity of domains and the concomitant increase in electron density contrast. It is at this temperature range that the two superstructures are seen in POM. Around $-1.4\text{ }^{\circ}\text{C}$, the narrow DSC transition indicated as “4” associates with the crystallization of fluorocarbon chains also seen in POM, DS and rheology as this is one of the main thermodynamic transitions. The transition is also manifested in the phonon propagation at hypersonic frequencies (Fig. 9, below) due to the density and compressibility change. At even lower temperatures, the small exotherm in DSC indicated as “5” is accompanied by a minor change in dielectric permittivity and hence assigned to the crystallization of the hydrocarbon chains. Lastly, at around $-55\text{ }^{\circ}\text{C}$ a very weak process is detected in DS, indicated as “6”, that associates with the complete freezing of all dipole motions, corresponding to the glass temperature of fluorocarbon chains.

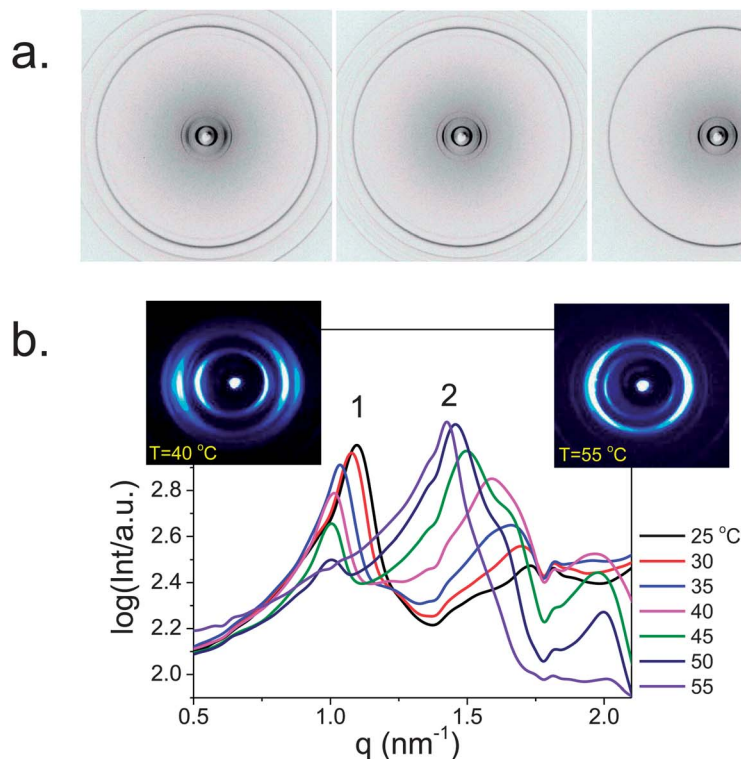


Fig. 5 (a) 2D-WAXS images of compound **3** at selected temperatures. From left to right: $-40\text{ }^{\circ}\text{C}$, $10\text{ }^{\circ}\text{C}$ and $20\text{ }^{\circ}\text{C}$. (b) 2D-WAXS images at $-40\text{ }^{\circ}\text{C}$ (left) and $55\text{ }^{\circ}\text{C}$ (right) and radially averaged profiles at different temperatures as indicated.

(b) Nano-structures and local dynamics

The 2D wide-angle X-ray images (Fig. 5a) display a set of reflections along the equatorial direction and another set in the meridional direction. Since the extruded fiber was held vertical and the X-ray beam directed perpendicular to the fiber axis, the equatorial reflections give the characteristic spacing of the lateral nano-phase separated hydrocarbon/fluorocarbon domains in a lamellar geometry. The first equatorial reflections at $-40\text{ }^{\circ}\text{C}$ can be described by the (100), (010) and (110)/(200) reflections from a simple rectangular unit cell with corresponding lattice parameters of $a = 5.07\text{ nm}$ and $b = 3.13\text{ nm}$. On the other hand, the set of meridional reflections is associated with inter-molecular correlations of hydrocarbon and fluorocarbon chains. The latter correlations melt at $20\text{ }^{\circ}\text{C}$ in accord with the DSC and DS results but the reflection at a characteristic distance of 0.48 nm persists up to $55\text{ }^{\circ}\text{C}$. This reflection originates from benzene–benzene interactions within the nano-domain rich in benzenes in a tilted arrangement (Fig. 2). Given its existence even at lower temperatures – despite with a lower intensity – we assume that some fraction of tilted domains exist down to $-40\text{ }^{\circ}\text{C}$.

Within the temperature range from 20 to $55\text{ }^{\circ}\text{C}$ two lamellae co-exist as shown by the 2D MAXS images in Fig. 5b. The two strong equatorial peaks correspond to lamellae with characteristic distances of 5.7 and 4.4 nm exceeding the molecular length ($\sim 3.6\text{ nm}$). A possible nanodomain morphology within this temperature range consists of two coexisting lamellae: one composed of tilted and fully extended fluorocarbon and

hydrocarbon chains (tilt angle estimated to be $\sim 40^{\circ}$) and another composed of non-tilted arrangement with nearly -but not fully- interdigitated chains (see Fig. 10, below). Above $55\text{ }^{\circ}\text{C}$, even the benzene–benzene interactions are overcome, suggesting a liquid-like behavior.

The viscoelastic properties of the different phases are plotted in Fig. 6. First isochronal measurements on cooling and subsequent heating are used to identify the phase transformations. The measured viscosity displays distinct steps on

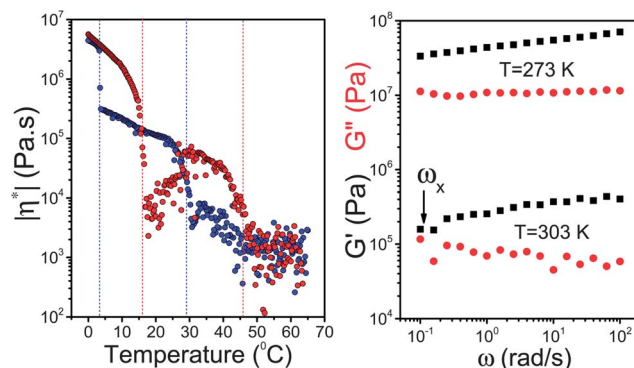


Fig. 6 (Left) Isochronal measurements of the shear viscosity on cooling (blue) and subsequent heating (red) at a frequency of 10 rad s^{-1} and a rate of $0.5\text{ }^{\circ}\text{C min}^{-1}$. The vertical lines indicate the transition temperatures. (Right) Frequency dependence of the storage (G' , squares) and loss (G'' , circles) moduli at two temperatures as indicated. The arrow indicates the characteristic frequency (ω_x) of structural relaxation at 303 K .

cooling corresponding to the nano-phase separated fluorocarbon/hydrocarbon domains (at $\sim 28^\circ\text{C}$) and the subsequent crystallization of the fluorocarbon chains (at $\sim 3^\circ\text{C}$). On heating, the pronounced melting of the fluorocarbon chains at $\sim 15^\circ\text{C}$ is followed by a broad temperature range where the viscosity displays a peculiar temperature dependence. It is within this range that the system is composed of two interchanging lamellae (tilted and non-tilted) and two superstructures (POM). The frequency dependence of the storage and loss moduli at two selected temperatures is also shown in Fig. 5. At 0°C , the moduli reflect the properties of the nano-phase separated fluorocarbon and hydrocarbon domains where, in addition, the fluorocarbon chains are crystalline. As expected, only restricted motions of the fluorocarbon chains are possible that give rise to the observed weak frequency dependence, *i.e.*, $G' \sim \omega^0$, $G'' \sim \omega^0$ with $G' > G''$. In fact a careful inspection reveals that $G' \sim \omega^x$ with $0 < x \ll 1$, suggesting a possible slow relaxation of the fluorocarbon chains. Below we will discuss the dielectric signal associated with this slow relaxation. On the other hand, at 30°C , the response is viscoelastic with a characteristic (slow) structural relaxation time (arrow in the figure) of the order of tens of seconds. The viscosity of **3** remains relatively high above 50°C in accordance with the slow kinetics.

Dielectric spectroscopy is a sensitive probe of the fluorocarbon environment during the phase transformations of compound **3**. Different partially overlapping processes are evident in the dielectric loss curves (Fig. 7) indicated as α^* , α' , α'' , δ process as well as a process at much lower temperatures (ϵ). In addition to the dipolar relaxations, ionic conductivity is also sensitive to structural changes displaying discontinuous changes at the phase transitions (arrows 3 and 4 in Fig. 7). Three HN functions were necessary to describe the dynamics. On

cooling from higher temperatures, a process called α^* appears at MHz frequencies with increasing dielectric strength that on further cooling splits into two closely spaced frequency processes, called α and α' . This occurs at about 55°C , *i.e.*, in the vicinity of the coexisting lamellae composed of tilted and fully extended fluorocarbon and hydrocarbon chains and of non-tilted but interdigitated chains. The two processes are attributed to the relaxation of fluorocarbon dipoles in the two different environments. Within this temperature range an even slower process exists, called the δ process, that is attributed to more cooperative relaxations of the fluorocarbon chains seen also in rheology. At about 1°C , the dielectric loss curves display a discontinuous decrease as a result of the crystallization of the fluorocarbon chains (arrow 4 in Fig. 7) that largely immobilize the dipole. At even lower temperatures another weak process (ϵ) but with a strong T -dependence is evident. This process is the low temperature relaxation identified in the isochronal measurements of Fig. 2 and 3 and reflects the complete freezing of the fluorocarbon dipole.

The dynamics of these processes is shown in an Arrhenius representation in Fig. 8. All processes are of cooperative nature as verified by the Vogel-Fulcher-Tammann (VFT) T -dependence, $\tau = \tau_0 \exp(B/T - T_0)$. Here, τ_0 is the relaxation time in the limit of very high temperatures, B is the activation parameter and T_0 is the "ideal" glass temperature located below the glass temperature T_g . For the α^* process the VFT parameters correspond to: $\tau_0 = 10^{-10}$ s (held fixed), $B = 1570 \pm 10$ K, $T_0 = 186 \pm 3$ K, for the α -process to: $\tau_0 = 2 \times 10^{-11}$ s, $B = 2000 \pm 30$ K, $T_0 = 166 \pm 9$ K, and for the ϵ -process associated with the complete freezing of the fluorocarbon dipolar dynamics to: $\tau_0 = 4 \times 10^{-3}$ s, $B = 1100 \pm 40$ K, $T_0 = 180 \pm 11$ K. For the α' and δ processes the smaller T -range precludes a reliable fit to VFT. In

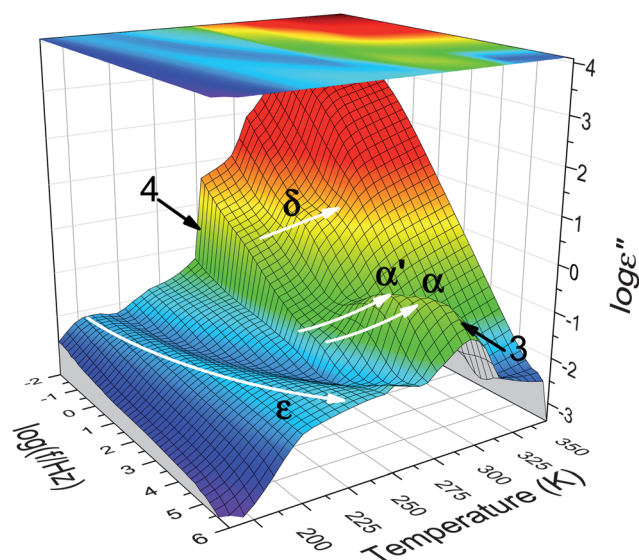


Fig. 7 Dielectric loss spectra of compound **3** in a 3D representation. The black arrows indicated as 3 and 4 give, respectively, the transition temperature corresponding to the coexisting lamellae and to the crystallization of fluorocarbon chains. The white arrows give the different relaxation processes indicated as α , α' , δ and a slower process (ϵ) associated with the glass temperature.

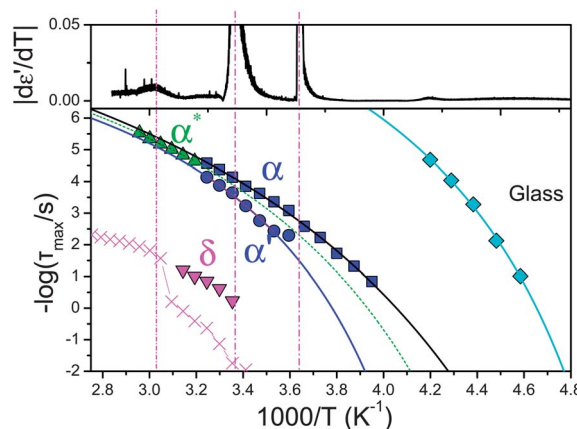


Fig. 8 (Top) Absolute derivative of the dielectric permittivity measured at $f = 1154$ Hz with a rate of 2°C min^{-1} as a function of inverse temperature. (Bottom) Arrhenius relaxation map of compound **3** depicting several processes: from high temperatures, the α^* -process (triangles) that splits into a "faster" α -process (squares) and a "slower" α' -process (spheres), the even slower δ -process (down triangles) and the low-temperature process associated with the freezing of the dipole moment at the glass temperature (rhombi). Solid and dashed lines are fits to the VFT equation. The process due to the ionic mobility (X) is also shown. Vertical dash-dotted lines indicate the transition temperatures obtained from the absolute derivative of the dielectric permittivity.

conformity with the relatively high viscosity (Fig. 6), the fastest relaxation time (for the α^* process) is only a few microseconds even up to $\sim 75^\circ\text{C}$ which might support metastability associated with the unexpected phase transformation revealed at high temperatures by DSC and DS (Fig. 4).

(c) Mesoscopic structures and metastability

A possible association of the high temperature DSC exothermic transitions (“1” and “2”) with an ordered viscous fluid would imply spatio-temporal fluctuations of the order parameter in analogy to diblock copolymers near the order-to-disorder transition. Since it is reasonable to assume elastic contrast, $\Delta Z = \Delta(\rho c_L)$ (see Section III) between such microregions, the existence should be manifested in the sound velocity, $c_L(T)$, at high frequencies where the system behaves elastically. In addition, if the phonon wavelength ($1/q$) is smaller than the spatial correlation of the microregions two distinct c_L 's are anticipated.²³ Probing different physical properties turns out to be important for elucidation of the behavior of complex molecular systems, as in the present case.

Fig. 9 displays the $c_L(T)$ of three samples of 3 treated differently as described in Table 2. The melting of the fluorocarbon block (regime I) around 5°C (at the rate of BLS experiment) and the intermediate temperature range up to about 45°C seems to be independent of thermal treatment. The former transition is associated with a rather small ($\sim 10\%$) drop of c_L corresponding to $\sim 20\%$ decrease of modulus. This weak decrease, which is in contrast to the large sharp peak in the DSC and viscosity at $\sim 0^\circ\text{C}$ (Fig. 4), implies that the density change upon melting of the fluorocarbon block is small. In the temperature range

$20\text{--}45^\circ\text{C}$, $c_L(T)$ decreases smoothly with temperature (regime II). This is associated with a structural transformation of lamellar arrangements of molten hydrocarbon and fluorocarbon blocks (Fig. 5). Only above about 45°C , $c_L(T)$ in sample B2 (green circles) drops below the solid line in Fig. 9 (regime III) and then assumes (in the two annealed samples) again the linear decrease with temperature above about 60°C (lower solid line); the equilibrium thermodynamic states are characterized by $c_L(T)$ represented by the three orange lines in Fig. 9. This broad transition (regime III) relates to the melting of the different crystalline structures as seen in the POM images in Fig. 1 and the loss of π - π interactions leading to a fluid-like lamellar structure. The transition regime indicated as III is broader than regime I and the sample becomes fully transparent only at about 60°C underlying the relation to macroscopic structures seen in POM. In view of the X-ray results, the clearing transition ($\sim 60^\circ\text{C}$) coincides with the temperature where the lamellar structures become fluid-like.

Unexpected is the observation of a much lower c_L in sample C compared to the value in the two annealed samples at temperatures above about 60°C . Also unexpected was the shift of regime III to higher temperatures. The very low c_L ($\sim 750\text{ m s}^{-1}$) at about 80°C falls well below the high temperature equilibrium line and is reminiscent of open structures. This metastable state, which is further indicated by the up-turn of $c_L(T)$ at $T > 80^\circ\text{C}$, is addressed while referring to Fig. 10. In fact, the as-prepared sample A1 (Table 2) shows very similar behavior with C (Fig. 9) but above 90°C its $c_L(T)$ increases abruptly and merges with the high temperature equilibrium line as seen by the comparison with the annealed B2 (green line) in Fig. 10. Interestingly, this metastability for as-prepared samples occurs in the temperature range of the peculiar high T peaks of the DSC trace (Fig. 1 and 3).

In order to examine a possible relation of this effect with the DSC dual transition (peaks 1 and 2), we examined the same sample by both techniques following a similar temperature protocol. The upper part in Fig. 10a displays the high temperature DSC traces for three cases as indicated in the plot. On heating the as-prepared B1 exhibits two (1 and 2) peaks, recorded (on-cooling) in Fig. 5, between 65 and 75°C . Annealing B1 at 50°C for 15 h has a strong impact on this transition by decreasing and merging the two peaks with a concurrent shift to lower temperature, as seen in the DSC trace (orange line) in Fig. 10a. The annealed B2 (Table 2) enhances this effect, *i.e.*, the broad DSC transition is weaker and shifts to 55°C . Turning to the BLS experiment, for the same as-prepared B1 sample the spectra in Fig. 10b (only the anti-Stokes side is shown) are single and shift to lower frequency with increasing temperature; $c_L(T)$ (solid red circles in Fig. 10a) displays the same $c_L(T)$ as for the as-prepared A1. At 77°C , which corresponds to the temperature at which the DSC peak 1 emerges, we recorded BLS spectra at different annealing times as indicated in Fig. 10b, while the time evolution of $c_L(T)$ is shown in Fig. 10c.

Three pertinent results emerge from the kinetic study of Fig. 10b. (i) A transient high c_L -state (open circle) coexistent with the slow c_L (solid circle) at early times, as seen in the double BLS spectrum in Fig. 10c. The high c_L ($\sim 1100\text{ m s}^{-1}$) falls on the blue

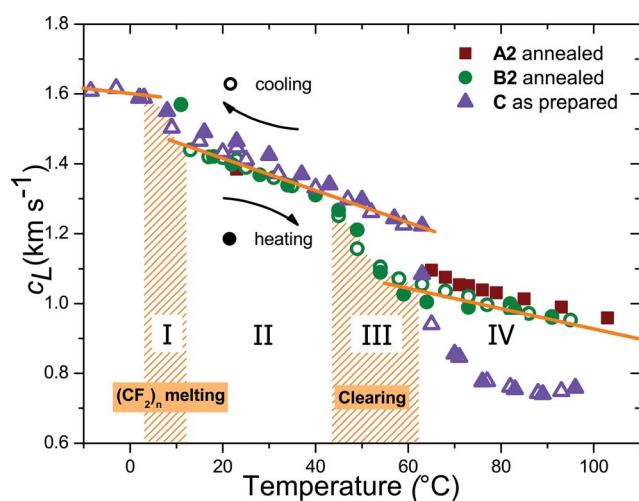


Fig. 9 Longitudinal phase sound velocity in the bulk material as a function of temperature for three samples (A2: squares, B2: circles and C: triangles) following different experimental protocols: non-annealed (C) and annealed (A2 and B2) samples. The solid lines denote limiting behavior at different physical states of the material: solid, liquid-crystalline and liquid going from low to high temperature. The shaded areas indicate the two transition regimes; melting of the $(\text{CF}_2)_n$ -block and clearing due to the melting of the structures of POM images in Fig. 1. Open and solid symbols are for measurements from high to low temperatures and vice versa indicated by the two arrows.

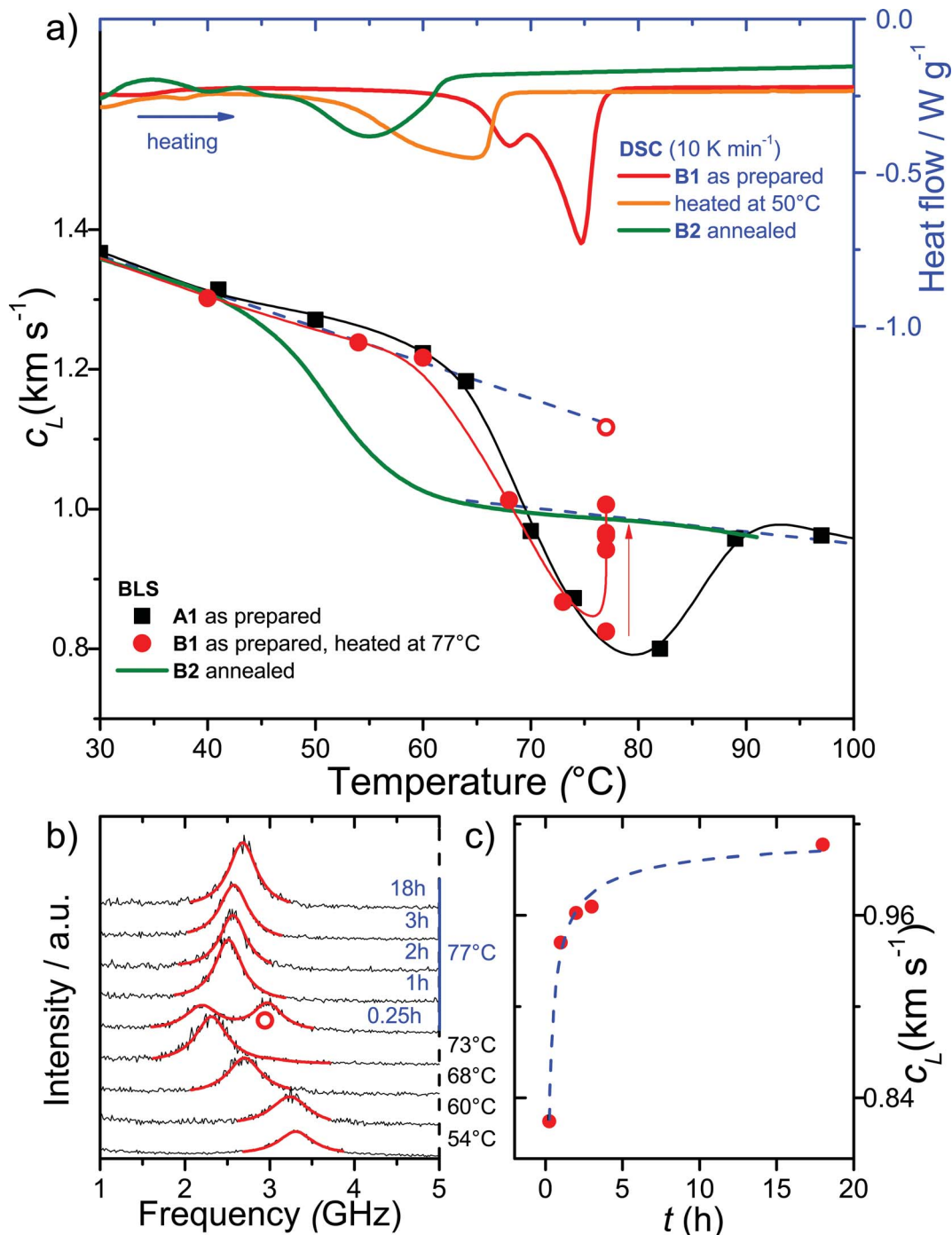


Fig. 10 (a) Longitudinal phase sound velocity c_L obtained from Brillouin Light Scattering (BLS) for three samples: as prepared (A1: squares and B1: circles) and annealed B2: solid line (from Fig. 9). For the as prepared sample B1, the kinetics of the transformation to the equilibrium state was examined at 77 °C indicated with the arrow. The BLS spectra of B1 and the variation of c_L with time at 77 °C are shown in (b) and (c) respectively. Differential scanning calorimetry (DSC) traces for A1, a fully annealed B2 and a sample heated at 50 °C for 15 h are shown in the upper part of (a).

dashed line in Fig. 10a which corresponds to the equilibrium regime II of Fig. 9, *i.e.*, the coexisting states of Fig. 5. As this coexistence is metastable (at 77 °C), the high frequency BLS peak is not discernible at longer times. On the other hand, the low c_L (~ 800 m s⁻¹), observed for as-prepared B1 and C, characterizes non-equilibrium open structures as already mentioned. The observation of two longitudinal phonons (at

early times) implies an inhomogeneous structure with correlation lengths larger than about 200 nm, the resolution length of the BLS. (ii) The low c_L metastable state, which is observed for all three (A1, B1 and C) as-prepared samples with the DSC trace of B1 (Fig. 10a), increases with time reaching the equilibrium liquid value (green solid line in Fig. 10a) after about 20 h (Fig. 10c). The slow transformation kinetics from a two-state

metastable liquid to the equilibrium system are supported by the relatively large viscosity (Fig. 6) and slow α^* -relaxation times (Fig. 7). (iii) The two DSC peaks and the drop of $c_L(T)$ in samples B1 (red lines) and B2 (green lines) emerge over a very similar temperature range as seen in Fig. 10a (both quantities recorded on heating). For the annealed B2 sample, the broad DSC trace falls into the T -range in which melting of the different crystalline structures as seen in the POM images in Fig. 1 occurs in conformity with regime III in Fig. 9.

The peculiar results of thermal annealing in the DSC traces and the longitudinal sound velocity within the temperature range from 55 to 90 °C can be understood as follows. From WAXS, we already know that at 55 °C the prominent benzene–benzene correlations are lost suggesting a liquid-like order of benzene rings. This is accompanied with the melting of mesoscopic structures in the POM images (Fig. 1), the emergence of transparency and the broad transition III in the elastic modulus (Fig. 9). Apparently, this weakening of interactions at the benzene-core allows some mixing between hydrocarbon and fluorocarbon chains. Within this temperature range, the system is prone to annealing (DSC, BLS) as kinetically trapped states can convert from locally segregated to more homogeneously mixed configurations; these configurations cannot be seen in WAXS as the domains are composed of both fluorocarbon and hydrocarbon chains with similar electron densities. The schematic of Fig. 2 is a compilation of the structural changes from different experiments.

4. Conclusions

A symmetrically tethered amphiphile to a benzene core analogous to SFAs provides the opportunity of synergistic self-assembly far more rich than any previously investigated SFA. The modulation of the intermolecular interactions between hydrocarbon and fluorocarbon chains as well as π – π interactions of the benzene cores are responsible for the rich self-assembly.

The structural features of compound 3 are summarized in a highly schematic way in Fig. 2. Starting from lower temperatures, distinct phases have been identified and their dynamics was explored. They consist of a low temperature lamellar phase (e) comprising nano-phase separated and crystalline fluorocarbon and hydrocarbon chains. Within this phase molecular mobility is practically frozen, thus the “phase” can be described as glassy. Upon increasing the temperature, phase (d) maintains lamellar-type but with melted hydrocarbon chains and crystalline fluorocarbon chains. At higher temperatures, phase (c) comprises coexisting lamellae of tilted and non-tilted molecules, the latter in a supramolecular arrangement (a smaller fraction of tilted molecules exist also at lower temperatures). Within this phase, both hydrocarbon and fluorocarbon chains are melted. The fluorocarbon chains display significant mobility as evidenced in DS by the dual VFT processes. Within the lamellar phases, π – π interactions are always present revealing that benzene cores are phase separated from the hydrocarbon and fluorocarbon chains. Increasing temperature induces a continuous transformation of these molecular and

supramolecular structures (X-rays, DSC, Rheology, BLS) resulting in mixed domains each composed of hydrocarbon and fluorocarbon chains. At this point (55 °C) the prominent benzene–benzene correlations are lost resulting in a fluid-like lamellar structure. This phase (b), which is different from the isotropic phase, is very prone to annealing (DSC, BLS) as kinetically trapped states can convert from locally segregated to more homogeneously mixed configurations. Lastly, at higher temperatures a quasi-isotropic phase is formed (a) composed of orientationally correlated dipoles (DS).

The present study revealed the key role of π – π interactions in the self-assembly of a semifluorinated benzene derivative. The orthogonal hydrocarbon/fluorocarbon and π – π interactions within the same molecule gave rise to self-assembly and metastability much more rich than in normal SFAs. Further studies on carefully designed amphiphiles with modulated interactions will shed more light on their self-assembly and metastability. Moreover, in view of the DS results, the nature of the isotropic phase in these semi-fluorinated compounds remains unclear. Studies addressing this issue are currently in progress.

Acknowledgements

The current work was supported by the Research unit on Dynamics and Thermodynamics of the UoI co-financed by the European Union and the Greek state under NSRF 2007-2013 (Region of Epirus, call 18). This work was co-financed by the E.U. – European Social Fund and the Greek Ministry of Development - GSRT in the framework of the program THALIS. Financial support by DFG Priority Program SPP1355 and the SFP 1459 is acknowledged.

References

- 1 J. G. Riess, *Tetrahedron*, 2002, **58**, 4113.
- 2 P. L. Nostro and S.-H. Chen, *J. Phys. Chem.*, 1993, **97**, 6535.
- 3 M. Hird, *Chem. Soc. Rev.*, 2007, **36**, 2070.
- 4 M. H. C. J. van Houtem, F. Benaskar, C. F. C. Fitié, R. Martín-Rapún, J. A. J. M. Vekemans and E. W. Meijer, *Org. Biomol. Chem.*, 2012, **10**, 5898.
- 5 A. N. Semenov, A. González-Pérez, M. P. Krafft and J.-F. Legrand, *Langmuir*, 2006, **22**, 8703.
- 6 J. F. Rabolt, T. P. Russell and R. J. Twieg, *Macromolecules*, 1984, **17**, 2786.
- 7 T. P. Russell, J. F. Rabolt, R. J. Twieg, R. L. Siemens and B. L. Farmer, *Macromolecules*, 1986, **19**, 1135.
- 8 J. Höpken and M. Möller, *Macromolecules*, 1992, **25**, 2482.
- 9 P. Marczuk and P. Lang, *Macromolecules*, 1998, **31**, 9013.
- 10 J. F. Rabolt and B. Fanconi, *Polymer*, 1977, **18**, 1258.
- 11 E. Núñez, C. G. Clark, W. Cheng, A. Best, G. Floudas, A. N. Semenov, G. Fytas and K. Müllen, *J. Phys. Chem. B*, 2008, **112**, 6542.
- 12 C. G. Clark, G. Floudas, Y. J. Lee, R. Graf, H. W. Spiess and K. Müllen, *J. Am. Chem. Soc.*, 2009, **131**, 8537.
- 13 M. M. Elmahdy, C. G. Clark Jr, H.-J. Butt, K. Müllen and G. Floudas, *J. Phys. Chem. B*, 2012, **116**, 13812–13820.

- 14 N. Audic, P. W. Dyer, E. G. Hope, A. M. Stuart and S. Suhard, *Adv. Synth. Catal.*, 2010, **352**, 2241–2250.
- 15 P. Bhattacharyya, D. Gudmunsen, E. G. Hope, R. D. W. Kemmitt, D. R. Paige and A. M. Stuart, *J. Chem. Soc., Perkin Trans. 1*, 1997, **1**, 3609–3612.
- 16 I. Fischbach, T. Pakula, P. Minkin, A. Fechtenkotter, K. Müllen, H. W. Spiess and K. Saalwächter, *J. Phys. Chem. B*, 2002, **106**, 6408.
- 17 F. Kremer and A. Schönhal, in *Broadband Dielectric Spectroscopy*, Springer, Berlin, 2002.
- 18 N. G. McCrum, B. E. Read and G. Williams, in *Anelastic and Dielectric Effects in Polymeric Solids*, Dover Publ. In., New York, 1991.
- 19 G. Floudas, Dielectric Spectroscopy, in *Polymer Science: A Comprehensive Reference*, ed. K. Matyjaszewski and M. Möller, Elsevier BV, Amsterdam, 2012, vol. 2.32, pp. 825–845.
- 20 S. Havriliak and S. Negami, *Polymer*, 1967, **8**, 161.
- 21 D. Schneider, F. Liaqat, El. H. Boudouti, Y. El Hassouani, B. Djafari- Rouhani, W. Tremel, H.-J. Butt and G. Fytas, *Nano Lett.*, 2012, **12**, 3101–3108.
- 22 R. C. Penciu, H. Kriegs, G. Petekidis, G. Fytas and E. N. Economou, *J. Chem. Phys.*, 2003, **118**, 5224–5240.
- 23 O. Priadilova, W. Cheng, G. Tommaseo, W. Steffen, J. Gutmann and G. Fytas, *Macromolecules*, 2005, **38**, 2321–2326.